EVIDENCE FOR X-RAY FLUX AND SPECTRAL MODULATION BY ABSORPTION IN NGC 6814. I. THE NATURE OF THE MOST RAPID VARIABILITY

KAREN LEIGHLY,[1,2] HIDEYO KUNIEDA,[3] YOSHIYUKI TSUSAKA,[3] HISAMITSU AWAKI,[3,4] AND SACHIKO TSURUTA[5]

ABSTRACT

The Seyfert 1 galaxy NGC 6814 was observed using the Japanese X-ray astronomy satellite *Ginga* in 1990 April and October. The rapid variability characteristically associated with this source was reconfirmed. Specifically, three dips were found in the April observation in which the flux dropped to nearly zero in ~ 300 s. The doubling timescale was ~ 50 s. A similar but separated drop and rise in flux was observed in the October data, different in that the flux did not decrease completely to zero.

A detailed analysis of the data around the structures of most rapid variability found spectral variability and lags in flux between different energy bands. Lags were on the order of a few to tens of seconds for the April data, and on the order of tens to a couple of hundred seconds for the October data. The sense of the lags was such that during flux decreases the hard flux lagged, while during flux increases the soft flux lagged. Associated significant apparent hardening of the spectrum at low flux was observed in the April data. Apparent hardening of the spectrum also occurred in the October flux decrease, to a photon index of $\Gamma = 0.85$; however, the spectrum softened at lowest flux to the index of the predecrease level, $\Gamma = 1.54$. In the April dips, the line flux was found to decrease significantly. A marginal decrease in line flux was also observed in the October data. The variability of the line flux reconfirmed the result of Kunieda et al. (1990), who found that the line producton region must be within ~ 300 light-seconds from the source.

To explain the observational results, a variable-absorption model was proposed, in which the column density was assumed to vary as a function of time. The time dependence of the column was determined in two ways. First, the functional dependence was assumed to be exponential, and model parameters were derived by fitting explicitly to the lag data obtained from the October observation. Second, a partial-covering spectral model was assumed, and the column density implied by the change in flux was found for both observations. The exponential folding time of the column density implied during the October flux decrease could be reliably determined to be about 100 s. The spectral variability could be qualitatively explained by the variable-absorption model, since superposition of continuously variable columns can result in an apparent hardening of the spectrum when measured by moderate-resolution instruments. The differences between the April and October observations could be explained if the two model parameters, the fraction of unabsorbed flux and the gradient with respect to time of the column density, were adjusted. Other physical processes, including intrinsic spectral changes and warm absorber models, which could account for the fastest variability, could be ruled out by the results of the data analysis. A primary constraint found for geometrical models is that the material which is doing the absorption must have relatively low ionization ($\xi < 100$). This result leads to severe constraints on a general orbiting cloud model, requiring high densities ($n \sim 10^{16}$ cm^{-3}) and sheetlike geometry.

Subject headings: galaxies: individual (NGC 6814) — galaxies: Seyfert — X-rays: galaxies

1. INTRODUCTION

The observation of rapidly variable Seyfert galaxies in X-rays can lead to important constraints on the nature of the central engine of active galactic nuclei (AGNs). This is because for radio-quiet sources the substantial emission in X-rays shows large-amplitude variation on shorter timescales than in other wavelength bands. For a timescale of substantial variability $\Delta\tau$, the source-size upper limit must be $R \sim c\,\Delta\tau$. A conventional picture of accretion-powered activity would have the bulk of the emission within $10r_S$, where r_S is the Schwarzschild radius (Shapiro, Lightman, & Eardley 1976). Therefore, the mass of the presumed black hole can be constrained.

NGC 6814 has been found to be the most rapidly variable Seyfert 1 galaxy in X-rays. In a study of 54 *HEAO 1* A-2 observations of 38 active galaxies, only NGC 6814 was found to vary on very short timescales of 100 s (Tennant & Mushotzky 1983). A remarkable dip was found in which the flux drops by a factor of ~ 6 in about 400 s (Tennant et al. 1981). Subsequent *EXOSAT* observations found an instance of rapid variability of more moderate magnitude with a timescale of about 500 s, as well as X-ray flares (Mittaz & Branduardi-Raymont 1989). A *Ginga* observation performed in 1989 April found the flux to fall by a factor of 3 in ~ 300 s, with a doubling timescale of only 50 s (Kunieda et al. 1990). Generally, other rapidly variable Seyfert 1 galaxies have been found to vary with substantially longer timescales of a few thousand seconds, including Mrk 335 (Turner & Pounds 1988), NGC 4051 (e.g., Kunieda et al. 1992; Matsuoka et al. 1990), NGC 5506 (McHardy & Czerny 1987), and MCG -6-30-15 (Pounds, Turner, & Warwick 1986; Matsuoka et al. 1990; Nandra, Pounds, & Stewart 1990). Thus it seems that NGC 6814 may be unique in its rapid variability.

[1] Code 666, X-Ray Astrophysics Branch, Laboratory for High Energy Astrophysics, NASA/Goddard Space Flight Center, Greenbelt, MD 20771.

[2] NAS/NRC Research Associate.

[3] Department of Astrophysics, Nagoya University, Furo-cho, Chikusa, Nagoya, 464 Japan.

[4] Current address: Department of Physics, Kyoto Univesity, Kita-shirakawa-iowake-cho, Sakyo-ku, Kyoto, 606 Japan.

[5] Physics Department, Montana State University, Bozeman, MT 59717.

Previously, the cause of the rapid variability was not known, and there were few clues. Significant systematic spectral variability was not confirmed during the most rapid flux changes (Tennant et al. 1981; Mittaz & Branduardi-Raymont 1989). Generally this is due to small detector areas and large statistical noise, preventing identification of spectral variability on short timescales.

In our current work using data from the large area counter (LAC) aboard *Ginga*, time-resolved analysis methods could be used to investigate the nature of the most rapid variability and constrain models for this phenomenon. Part of this work has appeared previously in Leighly (1991) and Leighly, Kunieda, & Tsuruta (1992).

In this work, § 2 describes the observations with the data reduction methods described in the Appendix. In § 3 are the results of time series analysis of the regions of most rapid variability. Flux lags of 1–2 hr have been measured from another Seyfert 1 nucleus NGC 5548 (Kaastra & Barr 1989), but here we report for the first time clearly significant lags on the order of tens to hundreds of seconds. Section 4 describes the spectral fitting results and demonstrates that significant spectral variability occurs during the rapid flux changes. Section 5 describes an innovative variable-absorption model which is shown to explain the analysis results. In § 6 analysis results are discussed, and other physical processes which have been used to explain spectral variability are shown to be inadequate. A general physical model is constructed, and the implications of the new results on several existing models for NGC 6814 are discussed. A summary is given in § 7.

2. THE OBSERVATIONS

Results from two *Ginga* observations of NGC 6814 are presented in this paper. The first observation was performed using eight LAC detectors on 1990 April 15–17. NGC 6814 was observed again using six LAC detectors on 1990 October 6–7, with an observation of background performed on October 5. Details of the data reduction are found in the Appendix.

Figure 1a shows the total flux light curve (1.11–20.9 keV) from the April observation. The zero of time corresponds to April 15 21:10:29 UT. The data from remote orbits of two days were available, separated by ~60,000 s. Because of pointing problems on the first day, only the data from the first orbit had transmission coefficient $T > 50\%$. The data from the second day, shown in the lower panel, were characterized by good transmission, $T > 90\%$. The peak flux was about 35 counts s^{-1} for eight detectors, while the lowest flux was nearly 0 counts s^{-1}.

Figure 1b shows the total flux light curve for the October observation. The zero of time corresponds to October 6 5:46:38 UT. Low background data were available only from one day; however, the transmission rate was high (>98%), and the gaps associated with Earth occultation and regions of high background were shorter, owing to favorable data selection conditions. The peak source flux was larger, being nearly 45 counts s^{-1} for six detectors. Therefore, the peak flux had nearly doubled when compared with the peak flux of the April observation.

The purpose of this paper is to investigate the nature of the most rapid variability. Therefore, the analysis described here focused on data from three orbits from the April observation and two orbits from the October observation. From the April observation, these are three dips, contained in orbits beginning at 0, ~86,000, and ~97,000 s from the beginning of the observation, and marked in Figure 1a.

There are no dips explicitly apparent in the October observation, but there are regions of rapid variability. A region of rapid variability contained in an orbit starting at ~22,500 s was examined, and is referred to as the "ingress." Careful examination of Figure 1b shows that the cusps of the dips are separated by multiples of ~12,000 s (Kunieda et al. 1991) and thus are apparently periodic. The periodic nature of NGC 6814 has been demonstrated previously (Mittaz & Branduardi-Raymont 1989; Done et al. 1992). Figure 1b shows a flux increase referred to as the "egress" contained in the orbit starting at ~11,000 s from the beginning of the observation. Examination of the figure finds that the times of lowest flux in the ingress and egress orbits are separated by about 12,000 s. Therefore, it may be that the ingress and egress are complementary parts of a dip structure, separated by one period.

3. TIME SERIES ANALYSIS

To investigate the variability during the rapid changes in flux, cross-correlations and template fitting of the light curve were used. Figure 2 shows the average dip data and the ingress and egress data in several different representative energy bands of 1.11–3.36, 3.35–5.69, 5.69–8.00, and 8.00–20.9 keV. Examination of this figure finds that lags and spectral variability are implied by the differing profiles in different energy bands.

In the following analysis, the ingress and egress regions of the October data were considered separately. Because of the low flux of the April data, the data from the three dips were averaged. To do this, the cusps of the dips were identified. We assumed that although there are only three dips, they are members of the same parent population, and therefore we calculate the average dip using the weighted mean and errors. An average dip data section of about 850 s in length resulted in which all three dips were represented. The dip profiles were not identical, and indeed varied significantly from the average dip profile. However, to investigate the spectral variability, the data are accumulated in several energy bands. In these separate energy bands, the dip profiles were found to be consistent with the average.

3.1. *Cross-Correlation Analysis*

Lags in flux between different energy bands can be seen in Figure 2. These lags can be quantified by calculating the cross-correlation of one energy band with respect to another. The algorithm used for calculation is that of Edelson & Krolik (1988), appropriate for unevenly sampled data. The form of the cross-correlation is shown in equation (1):

$$\text{CCF}(\tau) = \frac{1}{M} \sum \frac{(a_i - \bar{a})(b_i - \bar{b})}{[(\sigma_a^2 - e_a^2)(\sigma_b^2 - e_b^2)]^{1/2}} , \tag{1}$$

where the sum is performed over all M pairs for which the lag $\tau - \Delta\tau/2 \le \Delta t_{ij} \le \tau + \Delta\tau/2$. The symbols $\bar{a}$ and $\bar{b}$ denote the mean of distributions a and b, σ is the standard deviation of the data, and e is the average measurement error, which is included for the normalization of the CCF (Edelson & Krolik 1988). However, since only one orbit of data is considered at a time, the cross-correlation algorithm of Edelson & Krolik (1988) reduces to the classical discrete cross-correlation for evenly sampled data, with a sampling time of 16 s. Uncertainties are calculated according to the prescription of Edelson & Krolik
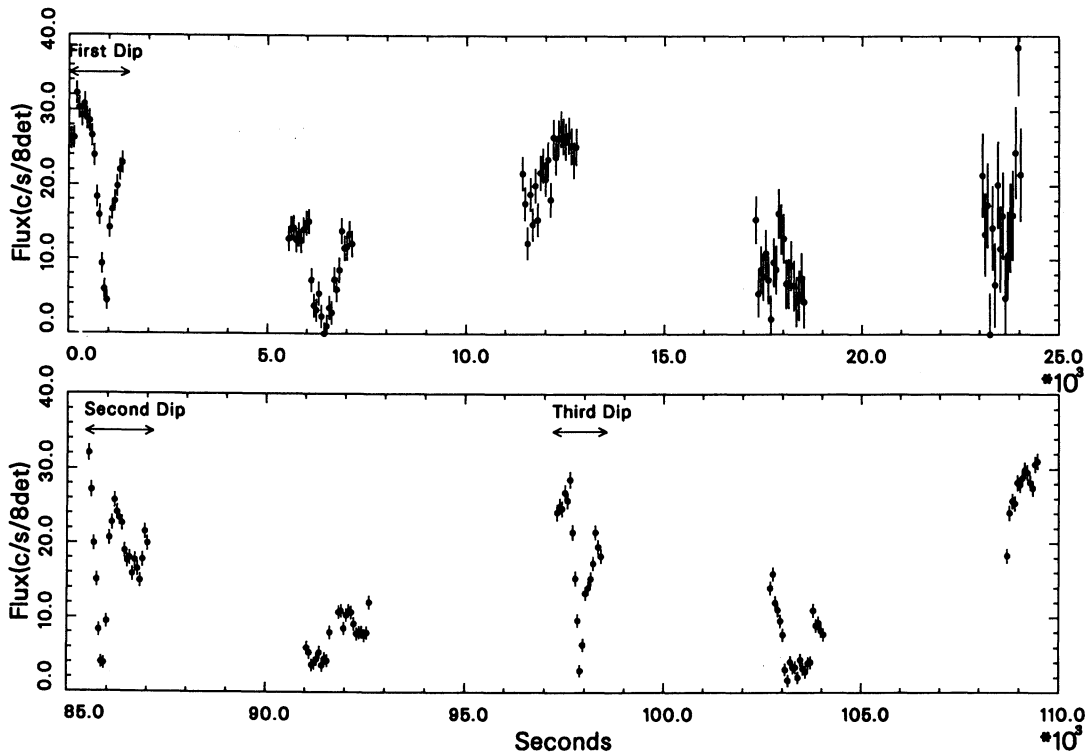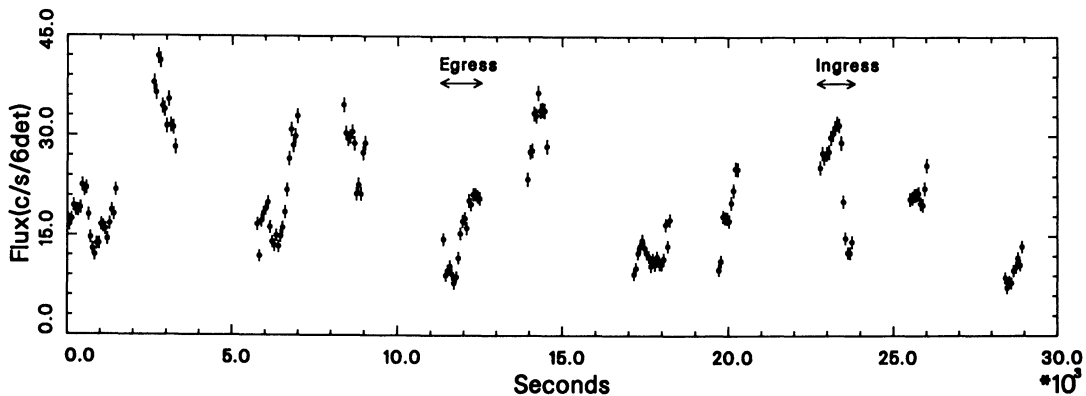
FIG. 1a

FIG. 1b

FIG. 1.—Total flux (1.11–20.9 keV) light curves. Time bin is 64 s. (a) April observation with the vertical axis showing counts s^{-1} for eight detectors, and marking dips. (b) October observation with the vertical axis showing counts s^{-1} for six detectors, and marking ingress and egress orbits.

(1988). An example of the cross-correlation from the October ingress data is shown in Figure 3.

For the cross-correlation analysis of the April average dip data, the data were divided and the ingress and egress regions analyzed separately so that the opposing lags would not average to zero. The representative energy bands considered are listed in the first column of Table 1. The cross-correlation of the hardest energy band light-curve data with each of the lower energy data with 16 s time resolution was calculated. Examination of the CCF in Figure 3 shows that it may be approximated by a Gaussian function offset from zero. Thus, the CCF was fitted with a Gaussian function,

$$\text{CCF} = C \exp\left[-\left(\frac{t - t_{\text{lag}}}{\sigma} \right)^2 \right] - 1 \,, \qquad (2)$$

where C is a constant describing the amplitude (≈ 2), t_{lag} is the lag, and σ is the width of the Gaussian. The uncertainties were evaluated assuming all parameters independent, and one parameter of interest. An example of the fit of the October data is shown by the solid line in Figure 3. Generally the fits were overdetermined, possibly because the errors are overestimated in the Edelson & Krolik method (Clavel et al. 1991).

The lags for the average dip ingress and egress are listed in column (2) of Table 1. For the average dip data from the April observation, small (less than 20 s) but significant lags were found. The sense of the lags was such that during flux decreases the hard flux lagged, while during flux increases the soft flux lagged.

In the cross-correlation analysis of the October ingress and egress data, seven energy bands for the ingress and six energy
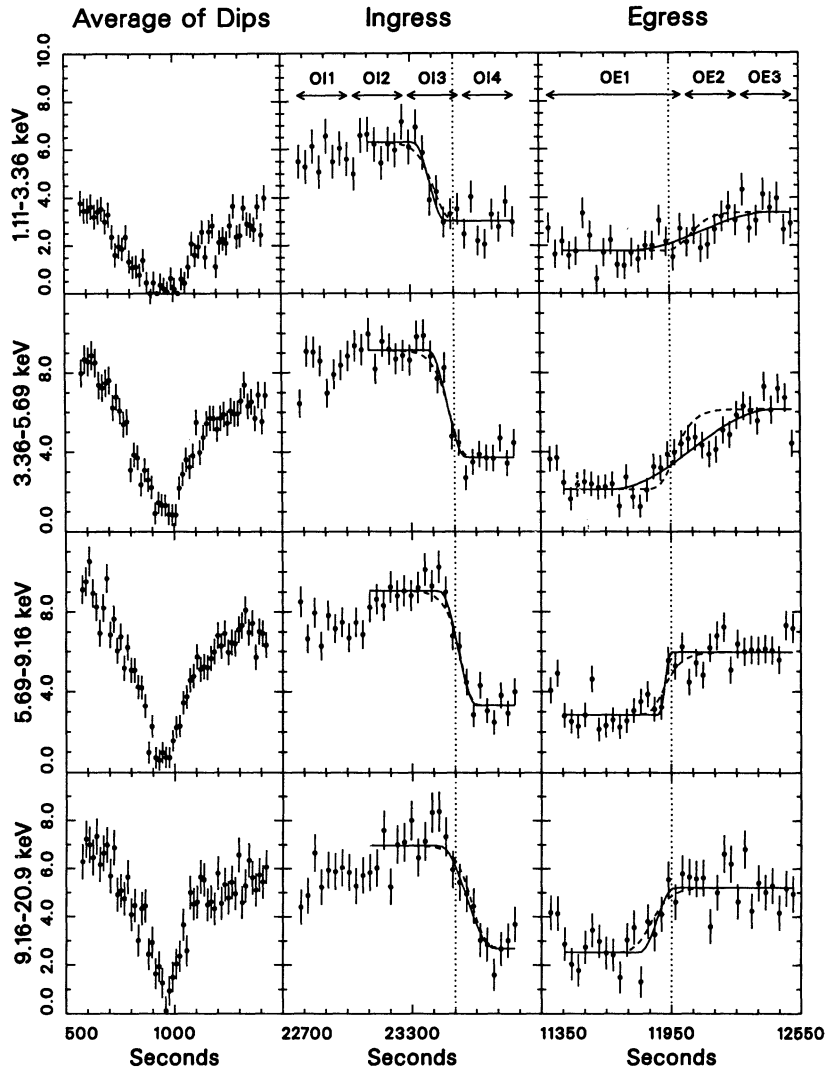
FIG. 2.—Light curves in several representative energy bands of the average April dip data, the October ingress data, and the October egress data. Vertical lines are provided for reference. Bin size is 16 s for the April data and 32 s for the October data. Dashed lines in the October ingress and egress light curves show the empirical segmented cosine fit. Dotted lines show the light curves predicted by the variable-absorption model.

bands for the egress were used as listed in Table 1. In contrast to the April dip data, very large lags, up to nearly 150 s, are found from both the ingress and the egress of the October data. The sense of the lags is consistent with the April dip data. Further, many of the energy bands show significant lags (1 σ) with respect to those bands adjacent in energy. For the October ingress data, note that the iron-line band (5.68–6.84 keV) does not show a large lag with respect to the highest energy band. In fact, the iron-edge band (6.84–8.00 keV) shows a larger lag. Also, the iron-edge band does not lead the 4.50–5.69 keV band significantly.

3.2. Template Fitting Analysis

Template fitting of the light-curve data to a function can be used to evaluate the lags independently. It is also useful because, when the CCF is used, if the lag is a large fraction of the length of the data section ($\sim 10\%$), end effects become important and the lag is underestimated. The length of the data sections containing the ingress and egress are ~ 1000 s, while the length of the data sections containing the dip increase and decrease separately is only ~ 400 s.

The template function which was used to model the increase or decrease in flux was a segmented cosine function:

$$y = \begin{cases} a \pm b, & t < \tau_H - \frac{1}{2}\tau_D, \\ b \pm a \cos\left[\dfrac{\pi(t - \tau_H + \frac{1}{2}\tau_D)}{\tau_D}\right], & \tau_H - \frac{1}{2}\tau_D < t < \tau_H + \frac{1}{2}\tau_D, \\ b \mp a, & \tau_H + \frac{1}{2}\tau_D < t. \end{cases} \tag{3}$$

This is a four-parameter model. The parameter a is the amplitude of the cosine, b is the offset from zero, τ_D is one-half the period of the cosine function, τ_H is the time at which the function falls or rises to the halfway point b, and the upper sign was used for the ingress, while the lower sign was used for the egress. The lags may be calculated from τ_H. Examples of the template fits to the light curves of the October ingress and egress are shown by the dashed lines in Figure 2.

The light curves from the average April dip data were fitted with the model. In this case only two of the segments of equation (3) were fitted, and the minimum of the cosine was fixed to
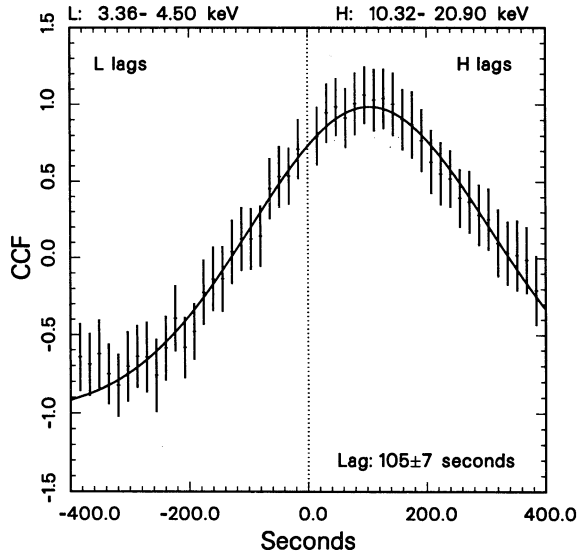
FIG. 3.—Example of cross-correlation function from the October ingress data. The solid line shows the best-fit Gaussian function, eq. (2). The time binning is 16 s.

TABLE 1

MEASURED LAGS

Energy Range (keV) (1)	CCF Lag[a] (s) (2)	Template Lag[a] (s) (3)
April Average Dip Ingress (10.32–20.9 keV)[b]		
1.11–3.36	16 ± 4	40 ± 21
3.36–5.69	14 ± 4	34 ± 17
5.69–8.00	6 ± 4	8 ± 17
8.00–10.32	9 ± 4	26 ± 23
April Average Dip Egress (9.16–20.9 keV)[b]		
1.11–3.36	−19 ± 6	−83 ± 19
3.36–5.69	−14 ± 5	−37 ± 9
5.69–9.16	−9 ± 44	−29 ± 8
October Ingress (10.32–20.9 keV)[b]		
1.11–3.36	125 ± 9	159 ± 27
3.36–4.50	110 ± 7	93 ± 25
4.50–5.69	57 ± 7	61 ± 25
5.69–6.84	16 ± 6	35 ± 25
6.84–8.00	54 ± 8	44 ± 29
8.00–10.32	2 ± 6	10 ± 30
October Egress (9.16–20.9 keV)[b]		
1.11–3.36	142 ± 12	−251 ± 53
3.36–4.50	−110 ± 9	−182 ± 54
4.50–5.69	−96 ± 10	−50 ± 32
5.69–6.84	−61 ± 10	−106 ± 59
6.84–9.16	−38 ± 9	−25 ± 25

[a] A minus sign indicates that the soft flux lags the hard, and uncertainties are 1 σ confidence with one parameter of interest.
[b] The range of energies used in the hard band, which was cross-correlated or compared with the softer energy bands listed.

TABLE 2

FIT RESULTS FOR THE TEMPLATE

Energy Range (keV)	τ_H[a] (s)	τ_D[a,b] (s)	χ^2/dof	Model[c] χ^2
April Average Dip Ingress				
1.11– 3.36.........	776 ± 16	...	18.9/22	...
3.36– 5.69.........	782 ± 9	...	15.0/22	...
5.69– 8.00.........	782 ± 9	...	36.5/22	...
8.00–10.32.........	790 ± 18	...	35.6/22	...
10.32–20.90.........	816 ± 14	...	21.6/22	...
1.11–20.90.........	792 ± 8	...	43.3/22	...
April Average Dip Egress				
1.11– 3.36.........	1125 ± 18	...	46.1/29	...
3.36– 5.69.........	1079 ± 7	...	27.4/29	...
5.69– 9.16.........	1071 ± 6	...	31.3/29	...
9.16–20.90.........	1042 ± 6	...	25.8/29	...
1.11–20.90.........	1068 ± 5	...	58.9/29	...
October Ingress				
1.11– 3.36.........	23391 ± 14	152 ± 75	17.0/18	19.1
3.36– 4.50.........	23457 ± 10	119 ± 52	15.9/18	16.2
4.50– 5.69.........	23489 ± 11	116 ± 59	18.4/18	20.1
5.69– 6.84.........	23515 ± 11	124 ± 56	19.6/18	24.3
6.84– 8.00.........	23506 ± 18	150 ± 93	25.3/18	25.4
8.00–10.32.........	23540 ± 20	251 ± 103	20.2/18	22.9
10.32–20.90.........	23550 ± 23	245 ± 114	21.2/18	23.8
1.11–20.90.........	23492 ± 7	210 ± 34	17.3/18	33.6
October Egress				
1.11– 3.36.........	12133 ± 49	355 ± 252	32.7/30	37.0
3.36– 4.50.........	12064 ± 50	783 ± 233	27.8/30	48.1
4.50– 5.69.........	11932 ± 25	232 ± 132	36.8/30	38.3
5.69– 6.84.........	11988 ± 56	855 ± 263	27.7/30	45.2
6.84– 9.16.........	11907 ± 15	103 ± 79	34.4/30	36.4
9.16–20.90.........	11881 ± 20	163 ± 110	37.7/30	40.7
1.11–20.90.........	11964 ± 27	583 ± 130	62.8/30	63.8

[a] Parameter uncertainties are 1 σ confidence assuming one parameter of interest.
[b] For the April data, $\tau_D = 2|\tau_H - 960|$.
[c] Light curves predicted by model compared with October data.

the phase of π at the dip minimum, determined to be 960 s. Therefore, for the April dip, $\tau_D = 2|\tau_H - 960|$. The results of the template fitting are listed in Table 2. From these, the lags were calculated and are listed in column (3) of Table 1.

The light curves from seven energy bands from the ingress and six energy bands from the egress were fitted with the model. Only part of the orbit light-curve segments were fitted, best representing the region over which the decrease or increase takes place. The fit results are listed in Table 2. The lags were calculated, and these are listed in Table 1. The values of τ_D and τ_H are plotted against energy in Figures 4 and 8, respectively.

Table 1 lists the lags as measured both using the cross-correlation and the template fitting method. The cross-correlation lags show smaller uncertainties than those calculated from the template fitting method. This is because the cross-correlation method essentially uses the hard-band light curve as a template, and thus this profile fits the lower energy light curves better than the empirical description given by equation (3).

The results from both methods are consistent for the smaller lag times measured. For larger lag times ($t_{\rm lag}$ greater than 10%
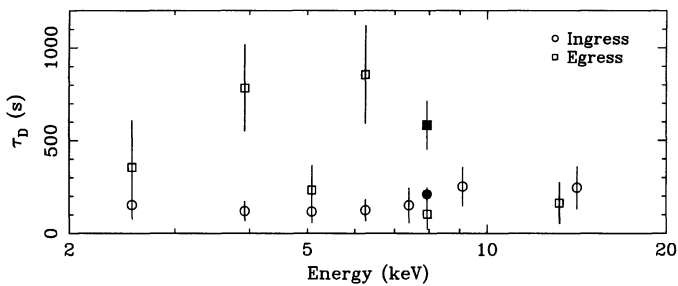
Fig. 4.—Template fit parameter τ_D versus energy for the October ingress and egress. The filled markers plot the parameter for the total light curve from 1.11 to 20.9 keV, while the open markers plot the parameter in different energy bands.

of the data-section length) the results are not consistent. This discrepancy can be attributed to the end effects in the calculation of the cross-correlation function. Also, for large lags fewer data points are contributing to the cross-correlation.

Another reason for the discrepancy comes from the fact that, for the cross-correlation calculation, all of the data in the orbit were used, including data from portions of the light curve not part of the flux increase and decrease. Since the spectrum is apparently not constant before the decrease, these data can only decorrelate the cross-correlation. Thus, the template fitting results are considered more reliable and are used for the remainder of the analysis.

The parameter τ_D listed in Table 2 and plotted in Figure 4 for the October ingress and egress data has a physical interpretation, describing the extent of the increase or decrease. The values obtained by the fitting although not well determined, are not consistent with a constant value. The values were generally smaller for the ingress data, with the hardest bands finding slightly larger values. For the egress the values for the softer bands were much larger, indicating a more gradual increase. For the total flux light curves, τ_D for the egress is significantly larger than for the ingress, indicating an overall slower increase.

4. SPECTRAL ANALYSIS

Further information about the nature of the most rapid variability can be discovered by examining the spectra in the regions of the April dips and the October ingress and egress. Spectra from the April dip data were first accumulated in 256 s bins and fitted with a power law plus line model as follows:

$$F(E) = [NE^{-\alpha} + N_{Fe} \text{ Line } (E, \Delta E, Z)]e^{-\sigma(E)N_H}, \quad (4)$$

where "Line" represents the Gaussian function. The width of the line is ΔE, fixed at 0.05 keV, and Z is the fixed appropriate cosmological redshift. The energy of the line was fixed at 6.4 keV. The errors calculated are at 90% confidence with one parameter of interest (Lampton, Margon, & Bowyer 1976).

Examination of the results from fitting the spectra with 256 s accumulation shows that some adjacent spectra are consistent with one another. Thus these could be combined for better statistics. In the final analysis 11 spectra were accumulated to describe the three dips. The spectral fitting results for these spectra are listed sequentially in Table 3, separated by dip number. As a group, the spectra from either before the decrease or after the increase are referred to as the "nondip" spectra, while those from the lowest flux regions are referred to as the "dip" spectra. The names of the spectra are coded to refer to the observation, the dip number, and whether the spectrum is composed of data from before (B), during (DIP), or after (A) the time of lowest flux. A final number (1 or 2) describing the position in time is appended when there is more than one spectrum before or after the lowest flux point.

In column (3) of Table 3 the best-fit photon index is listed. These values show a dramatic decrease in the dips, indicating a hard spectrum at the point of lowest flux. Because of the low flux of the dip spectra, the best-fit values are not well constrained. However, since the spectral fitting results of the dip spectra are consistent as a group, the three spectra from the April observation could be combined for improved statistics. The spectral fitting results for this combined spectrum are listed in the bottom line of the table. The photon index of

TABLE 3
Spectral Fitting Results for the April Dip Data

Spectrum (1)	Accumulated Time (s) (2)	Photon[a] Index (3)	log N_H[a] (cm^{-2}) (4)	Line Flux[a,b] (counts s^{-1}) (5)	Equivalent[a,b] (eV) (6)	χ_ν^2 dof (7)	Difference[c] in χ^2 Plot (8)	Flux[d] (9)
A1B1(b)	512	146 ± 0.17	22.70 ± 0.16	1.52 ± 0.50	490 ± 160	0.96/25	>90%	39.8
A1B2(b)	384	1.97 ± 0.22	23.03 ± 0.12	1.49 ± 0.66	440 ± 190	1.25/25	>99%	56.3
A1DIP(d)	256	1.03 ± 0.58	22.54 ± 0.87	<0.59	<630	1.61/26	...	9.6
A1A(a)	384	1.40 ± 0.22	22.67 ± 0.22	0.91 ± 0.56	360 ± 220	1.08/25	>1 σ	31.5
A2B(b)	256	1.51 ± 0.20	22.79 ± 0.16	1.55 ± 0.50	600 ± 190	0.73/25	>90%	34.4
A2DIP(d)	256	1.06 ± 0.49	22.32 ± 0.81	<0.64	<960	1.01/26	...	7.0
A2A1(a)	768	1.20 ± 0.10	22.42 ± 0.18	1.11 ± 0.23	530 ± 110	1.52/25	>1 σ	23.8
A2A2(a)	256	1.71 ± 0.21	22.94 ± 0.14	0.93 ± 0.51	400 ± 240	1.44/25	>90%	32.4
A3B(b)	512	1.51 ± 0.13	22.70 ± 0.14	1.13 ± 0.35	440 ± 130	1.40/25	>99%	33.4
A3DIP(d)	256	1.10 ± 0.38	22.71 ± 0.46	<0.39	<390	0.53/26	...	10.6
A3A(a)	384	1.27 ± 0.18	22.43 ± 0.32	0.77 ± 0.36	410 ± 190	0.48/25	>90%	22.1
ADIP(d)	768	1.03 ± 0.26	22.52 ± 0.41	<0.26	<290	1.15/26	...	9.1

Note.—In col. (1) (b) = before dip, (a) = after dip, (d) = dip spectrum.
[a] Parameter uncertainties are 90% confidence for one parameter of interest.
[b] Line energy was fixed at 6.4 keV.
[c] Smallest difference between the N_H photon index χ^2 contours for this spectrum and the ADIP spectrum.
[d] Continuum flux is from 2 to 10 keV, intrinsic, in counts s^{-1} for eight detectors.
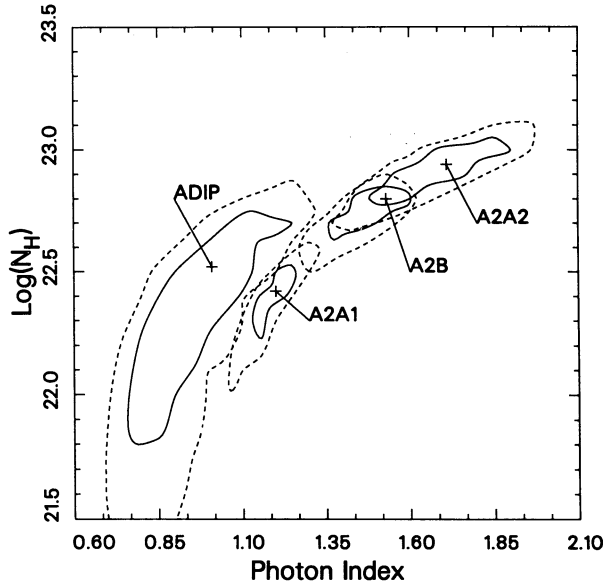
Fig. 5.—Example of χ^2 contours from the spectral fitting of the data around the second April dip, and the combined dip spectrum ADIP. The spectrum A2B occurred just before the dip, while the spectra A2A1 and A2A2 occurred sequentially after the dip. The solid line shows the contour of 1 σ confidence ($\Delta\chi^2 = 2.3$), while the dashed line shows the contour of 90% confidence ($\Delta\chi^2 = 4.61$) for two parameters of interest.

1.03 ± 0.26 is found to be very low, indicating a very hard spectrum. Column (4) gives the column densities, which do not vary as much as the photon index and tend to drop in value at the lowest flux.

Because of the coupling of the absorption column and index in the spectral fitting, the χ^2 contours must be examined to verify spectral variability. An example of the χ^2 contours for the combined dip spectrum and the nondip spectra of the second dip is shown in Figure 5. The contours shown are the 1 σ and 90% contours for two interesting parameters ($\Delta\chi^2 = 2.30$ and 4.61, respectively). These show that the combined dip spectrum is significantly harder than the nondip

spectra of the second dip, and marginally less absorbed. The contours from the combined dip spectrum were compared with those of all of the nondip spectra, and show significant spectral hardening in the dips compared with the nondip spectra. The confidence level of the difference is listed in column (8) of Table 3. In general, the spectra from before the dips differ from the combined dip spectrum by at least 90%, while the spectra from just after the dips differ from the combined dip spectrum by only at least 1 σ, illustrating a generally slower recovery. Thus, comparison of the χ^2 contours shows a significant spectral hardening in the dips compared with the nondip spectra.

Column (4) of Table 3 gives the line flux. The dip spectra did not require a line, and an upper limit was obtained. The upper limit for the combined dip spectrum at the 90% confidence level for one interesting parameter was only 0.26 counts s^{-1}. When the line flux parameter values of the nondip spectra are compared with this upper limit, it can be seen that they are significantly larger at the 90% confidence level. Therefore, these spectral fittings show that the line flux decreases significantly in the dips when compared with the nondip spectra.

The results of spectral fitting to the similarly combined spectra from the October ingress and egress data are found in Table 4. There are two groups of data corresponding to the ingress. The first four spectra correspond to all the data in the ingress orbit divided into equal parts. The last two spectra will be described subsequently in this section. The egress data were split into three spectra. The data accumulated for each spectrum are marked on Figure 2.

The results of spectral fitting to the October ingress and egress spectra are qualitatively similar to the results from spectral fitting of the April dip data. The index drops as the flux decreases and rises as the flux increases. Some of the best-fit spectral indices found were very hard, with photon indices below 1.0. The absorption column measured was generally somewhat smaller. In some cases, the absorption column[6] could not be determined, and it was necessary to fix the

---

[6] Recall that columns less than $N_H \approx 10^{21}$ cm^{-2} cannot be determined using *Ginga*.

TABLE 4

SPECTRAL FITTING RESULTS FOR THE OCTOBER INGRESS (OI) AND OCTOBER EGRESS (OE) DATA

Spectrum	Time Range Covered (s)	Photon Index[a]	log N_H[a] (cm^{-2})	Line Flux[a,b] (counts s^{-1})	Equivalent[a,b] Width (eV)	χ_R^2/dof	Flux[c]
			Ingress				
OI1	22784–23040	1.46 ± 0.16	22.46 ± 0.29	0.58 ± 0.47	210 ± 170	0.89/25	35.2
OI2	23040–23296	1.54 ± 0.16	22.34 ± 0.28	0.95 ± 0.49	320 ± 170	1.69/25	38.6
OI3	23296–23552	1.28 ± 0.16	22.62 ± 0.20	1.42 ± 0.51	460 ± 1.70	0.72/25	36.6
OI4	23552–23808	1.27 ± 0.28	22.27 ± 0.70	<0.41	<310	0.67/26	15.0
HARD	23488–23616[d]	0.85 ± 0.17	21.2(f)	0.89 ± 0.51	640 ± 370	0.59/26	14.5
SOFT	23616–23808[d]	1.54 ± 0.35	22.54 ± 0.43	<0.41	<320	0.76/26	16.6
			Egress				
OE1	11392–12032	0.85 ± 0.11	21.2(f)	0.77 ± 0.23	770 ± 230	0.47/26	10.5
OE2	12032–12288	0.99 ± 0.21	22.31 ± 0.47	0.98 ± 0.44	530 ± 240	0.71/25	19.9
OE3	12288–12544	1.39 ± 0.20	22.61 ± 0.25	1.14 ± 0.47	500 ± 200	0.82/25	28.6

NOTE.—The notation (f) means that the absorption column is fixed at the Galactic value.
[a] Parameter uncertainties are 90% confidence for one parameter of interest.
[b] Line energy was fixed at 6.4 keV.
[c] Continuum flux is from 2 to 10 keV, intrinsic, in counts s^{-1} for six detectors.
[d] These times are approximate (see text).

LEIGHLY ET AL.

column at the Galactic value of $N_{H(Gal)} = 10^{21.2}$ cm^{-2}. Also, in some of the low-flux spectra, the line model is not required. Line equivalent widths are very large, especially for the low-flux egress spectra. Even with the higher flux of these spectra, because of the more gradual change in spectrum, it cannot be shown that adjacent spectra are significantly different, as was possible with the April data.

Spectral fitting of the April dip and October ingress and egress data seems to find that the spectral index is correlated with the flux. The softness ratio along with the 1.11–5.69 and 5.69–20.9 keV light curves for the ingress are shown in Figure 6, with data binning of 64 s. This figure shows that the last three points in the light curve are relatively soft, approximately as soft at those before the decrease. The spectral fitting results of the four ingress spectra marked on Figure 6 do not reflect the softening expected from the softness ratio light curve because the spectrum at low flux is composed of the last four points in the light curve, and hard and soft spectra are averaged. To demonstrate the softening at low flux, essentially the last three points shown in Figure 6 were accumulated into a spectrum labeled SOFT. The actual data selection for this spectrum was such that the count rate of the 8.00–20.9 keV band should be between 0 and 5 counts s^{-1}. For comparison, another spectrum labeled HARD was made, selected to be between 5 and 8.5 counts s^{-1} in the same energy band. This spectrum was composed essentially of the previous two points and is also marked on Figure 6. Although the SOFT and HARD spectra were composed of only 192 and 128 seconds, respectively, because of the reasonable flux (~ 10 counts s^{-1}) the spectral fitting results are reliable.

Spectral fitting results of these two spectra are listed fifth and sixth in Table 4, and the fits are shown in Figures 7a and 7b. As predicted, the HARD spectrum is significantly flatter, with a photon index of 0.85 ± 0.17, while the SOFT spectrum is steeper, with a photon index of 1.54 ± 0.35. Comparison of the χ^2 contours shows that the spectral variability is confirmed at only

the 1 σ level. Although this shows that spectral variability is only marginally significant, it is remarkable for spectra of such small accumulation times, and on such a short timescale of 128 s. The spectral index of the SOFT spectrum shows that, as predicted by the softness ratio of Figure 6, the spectrum returns to its predecrease level at lowest flux. Note that the fluxes of the HARD and the SOFT spectra are nearly the same.

There are some other interesting features in these spectra. For the HARD spectrum, the column density fit found the upper limit of the Galactic N_H, as is the case for the hardest spectra from the egress. Also, the HARD spectrum required an iron emission line. In contrast, the following SOFT spectrum did not require a line, and the upper limit was found showing a marginally significant difference at better than 1 σ confidence compared with the fit from the HARD spectrum. Interestingly, the equivalent widths are different at the 90% confidence level. The equivalent widths found for some of the low-flux spectra are very large, as large as 770 ± 230 eV. This result contradicts the results of Kunieda et al. (1990), who find that for spectra sorted by total flux the equivalent widths are consistent with a constant. As will be discussed in the next section, this result is likely an artifact of the absorption and does not imply an actual physical increase of the equivalent width.

5. THE VARIABLE-ABSORPTION MODEL

The dips in the April light curve, in which the flux drops to nearly zero, suggest an appropriate model to explain the most rapid variability. A most obvious model which can explain the change in flux is a simple absorption model in which material optically thick to X-rays comes between the observer and the source and temporarily blocks the X-ray flux. The drop and recovery of the October ingress and egress regions can also be explained if the source is only partially occulted. Although this simple absorption model can explain the change in flux observed, it cannot adequately explain the flux lags and spectral hardening observed in the regions of most rapid variability.

Therefore, a modified absorption model is proposed to describe the most rapid variability in NGC 6814. This model is a variation of the partial-covering model, but the column density of the partial coverer is assumed to be a variable function of time. This mechanism takes advantage of the fact that the X-ray photoelectric absorption by cold material with cosmic abundance is energy-dependent (Morrison & McCammon 1983). The lags observed can be explained if the column density increases as the time increases. During a flux decrease, first the soft flux is absorbed by a relatively small column density. As the column increases, harder flux is absorbed. The amount of lag measured directly implies the gradient of the column with respect to time.

In the next section we postulate that a two-parameter exponential model can describe the variation of the column density as a function of time. Then we fit the hypothesized model to the τ_H results from the template fitting of the light curve. This procedure makes explicit use of the fact that flux lags are observed. The light curves predicted by this model are compared with the measured light curves. In the following section the column density is derived in an alternative way: we assume a partial-covering spectral model, and then derive from the light curves directly the implied column density as a function of time for a fixed covering fraction. The log of the column density for the October ingress and egress is found to be a linear function of time, justifying the choice of the exponential
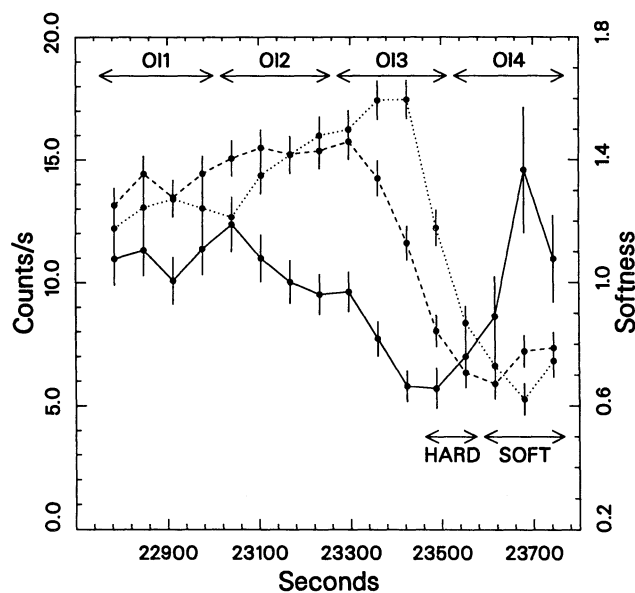

FIG. 6.—Light curves from the October ingress data, with time bin 64 s. The dotted line shows the light curve in the energy band 5.69–20.9 keV, the dashed line shows the light curve in the energy band 1.11–5.69 keV, and the solid line shows the softness ratio. Data uncertainties are 1 σ. The ingress spectra are also marked.
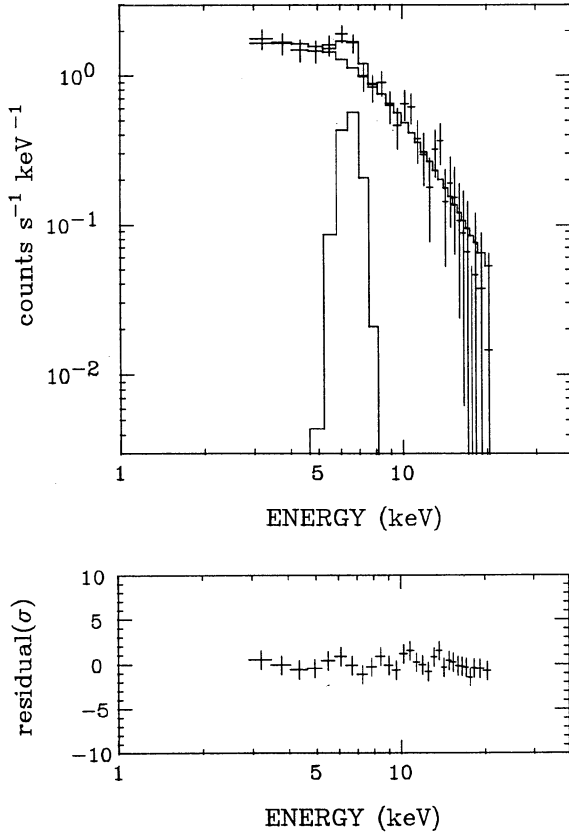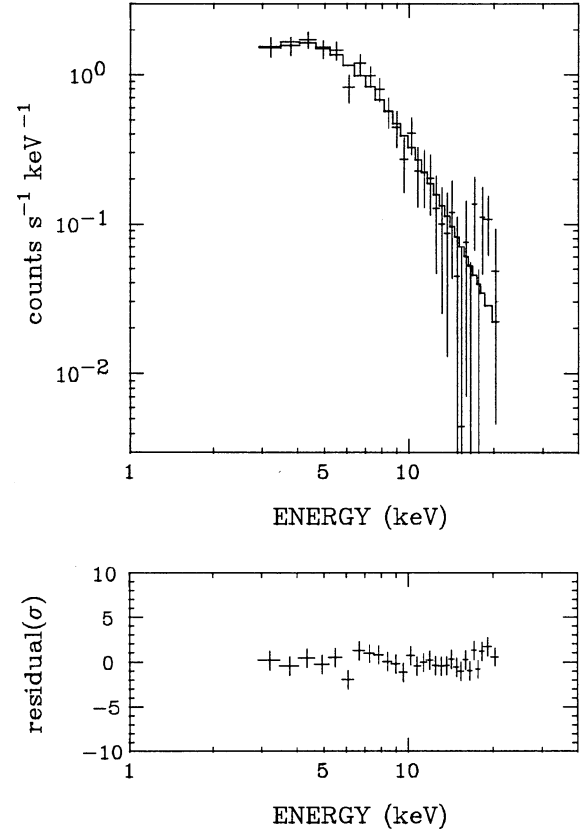
Fig. 7a

Fig. 7b

Fig. 7.—Spectral fitting results from the ingress (a) HARD and (b) SOFT spectra

function in § 5.1. The timescales for the flux and column to change are evaluated. Finally, the spectral variability is discussed in the context of this model, and simulations are presented which show that it can explain qualitatively the spectral variability observed.

5.1. *Lag Fitting of the Empirical Model*

In this section we use the template fitting results to fit a model which describes the column density covering the source at a given time, $N_H(t)$. We assume that the fraction of this material covering the source remains constant. The fit parameter τ_H can be used, because it is the time at which the flux varies halfway from its initial value to its final value. The time for this to happen can be easily found for any model of the column density, as follows.

If no additional absorption by the host galaxy is assumed, then the maximum flux is given by

$$F_{Max} \propto \exp\left[-\sigma(E)N_{H(Gal)}\right],\qquad(5)$$

where $\sigma(E)$ is the energy-dependent absorption cross section and $N_{H(Gal)}$ is the absorption column due to the Galaxy. The values of the cross section for neutral material given by Morrison & McCammon (1983) were used. The time $t_{1/2}$ at which the flux changes by half the distance between its initial level and final level obeys the equation

$$F(t_{1/2}) \propto \exp\left\{-\sigma(E)[N_{H(Gal)} + N_H(t_{1/2})]\right\},\qquad(6)$$

where $N_H(t)$ is the time-independent additional column covering the source. Setting equation (6) equal to one-half of equation (5) results in the following equation:

$$N_H(t_{1/2}) = \frac{-\ln(0.5)}{\sigma(E)}.\qquad(7)$$

For simple models of $N_H(t)$, this equation can be solved explicitly for $t_{1/2}$.

We hypothesize that a two-parameter exponential model can describe the time-dependent column density $N_H(t)$. The model equation used was

$$N_H(t) = 10^{\pm[22+(t-t_{22})/\tau_F]} \text{ cm}^{-2},\qquad(8)$$

where the plus sign is for the ingress and the minus sign is for the egress. There are two fit parameters in this functional form: t_{22} is the time when the column density is equal to 10^{22} cm^{-2}, and τ_F is the folding timescale for the column to change by a factor of 10.

The τ_H values from the template fitting listed in Table 2 are used to determine the fit parameters t_{22} and τ_F. Since these values were found by fitting light curves accumulated over a range of energies, the energies chosen to correspond to the τ_F values were found by calculating the mean of $E^{\Gamma-1}$, assuming $\Gamma = 1.54$, weighting with the approximate detector effective area (Makino et al. 1987), and folding in the Galactic absorption.

To fit the function, the model distribution of N_H given in equation (8) was used in equation (7), and the model values of $t_{1/2}$ were computed for the same energies using trial values of t_{22} and τ_F. These times were compared with the experimental

LEIGHLY ET AL.

TABLE 5

MODEL FIT RESULTS

Data	τ_F[a] (s)	t_{22}[a] (s)	χ^2/dof
Lag Fitting			
October ingress................	97.8 ± 16.6	23360 ± 390	3.4/5
October egress.................	113.8 ± 34.8	17210 ± 860	10.1/4
Light-Curve Fitting (Linear)			
April average dip ingress......	106^{+20}_{-14}	653^{+27}_{-35}	3.9/22
April average dip egress.......	149^{+23}_{-32}	1272^{+31}_{-27}	14.2/28
October ingress................	104^{+25}_{-17}	23356^{+28}_{-37}	3.2/12
October egress.................	230^{+72}_{-44}	12299^{+176}_{-98}	4.8/22
Light-Curve Fitting (Exponential)			
April average dip egress.......	157^{+160}_{-60}	1170^{+270}_{-80}	5.1/27

[a] Parameter uncertainties are 1 σ confidence for two parameters of interest ($\Delta\chi^2 = 2.3$).

values using the χ^2 statistic, and the values of t_{22} and τ_F were adjusted until the statistic was minimized. The fit results for the October ingress and egress data are given in Table 5, and the data plus model are shown in Figure 8.

The fit was overdetermined for the ingress data ($\chi^2 = 3.43/5$ dof), illustrating the appropriateness of the model. The bend in the model is due to the discontinuity at the iron absorption edge (Morrison & McCammon 1983). The data are fitted well in this region, since the point at ~ 6 keV corresponds to larger $\tau_{1/2}$ than the point at ~ 7.5 keV. Thus, this model predicts the result observed in the cross-correlation analysis, that the iron-line band data point at ~ 6 keV should not be greatly lagged from the highest energy band, while the iron-edge band point at ~ 7.5 keV should be more lagged (see Table 1).
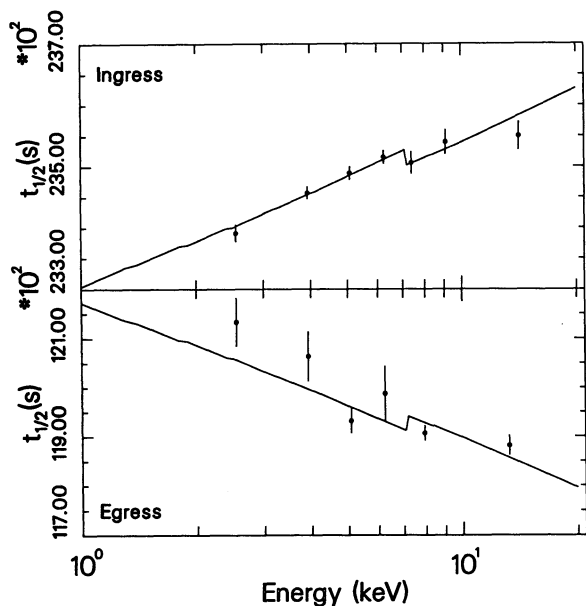

FIG. 8.—Results of fitting with variable-absorption model. The vertical axis shows the time at which the flux reaches the level half of the distance from its initial value to its final value. For the ingress, χ^2 was 3.4 for 5 dof, while for the egress χ^2 was 10.1 for 4 dof. Data uncertainties shown are 1 σ.

This fit is not satisfactory for the egress data ($\chi^2 = 10.1/4$ dof). The problems with this fit probably lie in both the model and the data.

With respect to the data, it cannot be certain that in the orbit comprising the egress the entire flux increase is seen, owing to the data selection which may interrupt the increase before the light curve levels out. Then, the time when that flux rises to one-half of the total flux will be estimated incorrectly, and the value of τ_H for softer bands could be larger. Also, the segmented cosine function is not always a good description of the light curves for the egress, as seen in Figure 2.

With respect to the model, first, there is no reason that the form of the empirical model should be a good description of both the ingress and egress data regions, although the calculation in the next section shows by an independent method that it is justified. Second, since there is residual flux at lowest flux in the October data, an extended source is implicitly assumed. Thus it may be that the column varies in the spatial as well as the time direction. Besides the poor fit, there is additional evidence that such spatial variability may be present. Recall that the τ_D parameter measured in the template fitting and describing the extent of the decrease is not consistent with a constant for all of the egress light curves. Specifically, the soft bands show a slower increase than the hardest bands. If the variation occurs only as a function of time, as the model in equation (8) requires, τ_D should be constant. Since τ_D is not constant, the N_H must be distributed spatially over a source with finite size. Since the model only considers variability with respect to time, a poorer fit results. However, it is clear that lags are present, and a more complex model having more free parameters could be found which would fit the data better.

The values of the two model parameters were not well determined by the data. Table 5 lists the 1 σ uncertainty assuming two parameters of interest. These show that the folding time-scales τ_F are consistent with one another, although the egress value is larger. Thus it cannot be claimed, using this method, that the gradient of column density with respect to time is smaller for the egress compared with the ingress, although such a result is suggested.

In general, the model fits the data extremely well despite its simplicity.

5.2. Light Curves Predicted by the Model

The light curves predicted by the model were calculated and are given by the dotted lines in Figure 2 for the energy bands shown there. These light curves were normalized to the best-fit asymptotic values from the segmented cosine model. In addition, the χ^2 values measuring the consistency of the data with the simulated light curves are listed in Table 2. The agreement between the model light curves and the data is generally acceptable for the ingress and the model χ^2 is comparable to the empirical segmented cosine fit χ^2. For the egress, the fit is generally worse, especially for the softer bands. The softer data show a slower increase than the predicted light curves. Again, this may be because a model containing N_H as a function only of time is not a good fit for the region.

Again note that the model calculation assumed a point source, an assumption shown in the last section to not be completely self-consistent. If the column density is assumed to be variable in the spatial direction as well as the time direction, a finite source size must be assumed. If the source size is finite in the time direction, the predicted light curves will vary more slowly in the region of the flux change. This will fit the soft
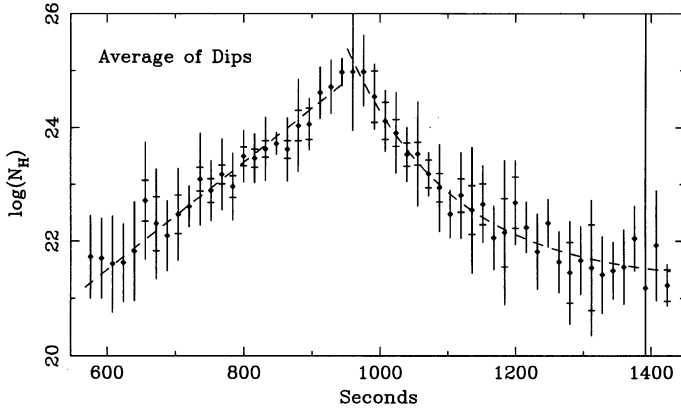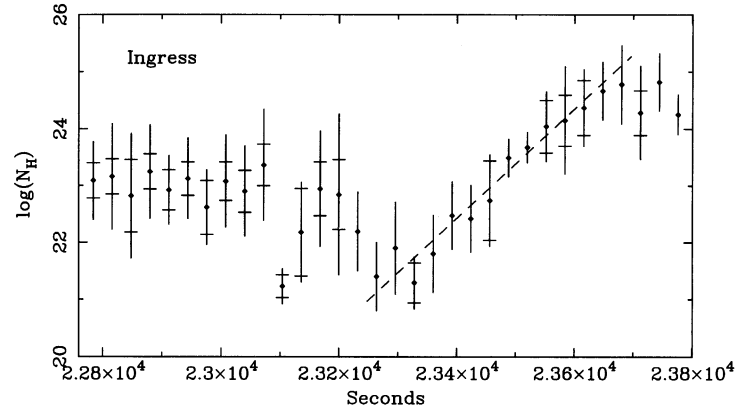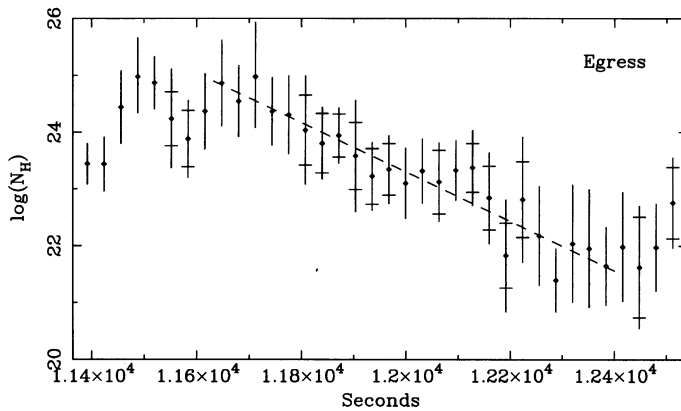
FIG. 9a

FIG. 9b

FIG. 9c

FIG. 9.—Column densities as a function of time for (a) the averaged April dip data, (b) the October ingress, and (c) the October egress as derived from the light curves directly. When two error bars are shown, the larger is the maximum error bar, computed from the best fit when the errors on N_H as determined from different energy bands are increased uniformly until the fit is overdetermined at the 90% level. The smaller bars result from the fit before the error bars were increased. Dashed lines show best fits, linear for the October data and the April dip ingress, and exponential for the April dip egress.

bands of the egress, but may not fit the ingress data if the source is assumed to be very large.

If the material is composed of small clumps, the requirement of an extended source can be relaxed.

5.3. Absorption Measured from the Light Curves

In the previous section the variable absorption column was determined from the template fitting of the ingress and egress light curves using an assumed exponential model. However, this is an empirical model for the variable absorption column. In this section we assume a spectral model and use the light curves and the asymptotic results from the template fits to find the implied variable column as a function of time directly.

If the spectrum has the form of a partially covered source, with the column density of the covered section varying with time, then the light curve can be written as

$$F(E, t) = F_0(E)(1 - f)e^{-\sigma(E)N_{H(Gal)}} + F_0(E)fe^{-\sigma(E)[N_{H(Gal)} + N_H(t)]} .$$

(9)

The fraction of the source covered is $f = 2a/(a + b)$ in terms of the template fit variables of equation (3). For the total flux light

curves for the ingress and egress, the fraction is close to 0.57 in both cases. For the April data the fraction was about 0.84.

To use this information to find the column density, spectra were simulated from this model using XSPEC for a range of values of $N_H(t)$. The spectra were rebinned with the same energy binning as the light curves. From these simulated spectra, the fractional decrease in flux as a function of column density and energy bin were obtained.

The data were renormalized using the template fit results so that each light curve would vary between 1 and $1 - f$, and would imply the same covered fraction. The uncertainties of the data were increased appropriately according to the uncertainty on the template fit results.

The light curves were then compared with the flux decrease curves obtained from the simulations, and the appropriate column for the fractional decrease of the light curve was obtained for each energy band at each point. Likewise, the uncertainties on the columns were obtained from the uncertainties of the light curves. In the case in which the point was larger than 1, the column implied was assumed to be the Galactic column $N_H = 10^{21.2}$ cm^{-2}, and in the case in which the point was less than $1 - f$, the column was assumed to be the maximum considered, $N_H = 10^{25}$ cm^{-2}, which is effectively thick for X-rays with energies less than 20 keV. In these two cases the error assigned was log $N_H = 3.8$.

The light curves in each energy band provided a measurement of time-dependent column which was derived essentially from the change in flux. There must be lags in the data for these estimations to be consistent between energy bands. The low-energy light curves could not provide information about large columns, and likewise the high-energy light curves could not provide information about small columns. To find the best estimation of the column implied, the data from all of the light curves were fitted with a constant column density model at each time. The results are shown in Figure 9a for the averaged dips, in Figure 9b for the ingress, and in Figure 9c for the egress.

At some times two error bars are shown. This is because the constant-column hypothesis did not result in a good fit in all cases, and the error bars found an underestimation of the uncertainty. So the error bars for such times were increased by a constant so that the fit to the constant column would be overdetermined at the 90% confidence level. The error on $N_H(t)$ calculated from that fit gives the maximum uncertainty expected.

Most of the fits were acceptable at the 90% confidence level.

For the average dip data only 10 of the 54 points were not. For the ingress, of the 32 time points shown, only eight were unacceptable. Six of these occur for times less than 28,600 s, and the poor fit, plus the larger column found, are probably due to the fact that the template fits were not performed in this region but were started from $t > 28,600$ s. For the egress data, all of the fits were acceptable at the 90% confidence level.

The column densities as a function of time were fitted with a straight line. The results are listed in Table 5 in terms of the variables of equation (8) and plotted in Figure 9. For the dip egress the straight-line fit was acceptable, but a better fit was found using an exponential function. Since the log of the column is plotted, the straight-line fit shows that the assumption of § 5.1 of an exponential time variability was justified. The leveling off of the ingress curve for large t may not be real but is probably due to the inability of this method to determine very large column densities.

5.4. *Timescales of Flux and Column Change*

From these results we can determine two physical parameters. The flux change timescale can be used to determine the extent of the optically thick material covering the source, and the column change timescale can be used to determine the extent of the optically thin material covering the source.

5.4.1. *Flux Timescale*

The timescale for the flux to change can now be determined in three ways. First, it can be determined from τ_D, the template fit parameter, for the total light curve. This determination takes into account only the flux decrease, and does not address the possibility that the covering material may have variable column density. The accuracy of the τ_D determination depends mostly on the accuracy of the template fitting. Second, the flux change timescale can be determined from τ_F measured from the lag data. This determination takes into account only the fact that the data is lagged but does not address the possibility that the covering fraction may not be constant. The accuracy of this depends mostly on how accurately the template fit parameter τ_H can be determined, and how appropriate the empirical function chosen to describe the column density variability is. The final method is through fitting the column density versus time as determined from the light curves. The column determination is driven mostly by the flux variability, and the column variability determines the error bars. A basic assumption of this method is that the covering fraction is constant, which will not affect the magnitude of the flux change timescale but will affect the uncertainties. The renormalization of the light curves depends on the template fitting through the asymptotic parameters.

The timescales of decrease for the two methods applicable to the April dip egress data give roughly consistent values. The timescale is roughly 300–500 s. For the October and April ingresses, the τ_D timescale is significantly shorter (~ 210 s) than the decrease timescales determined through the other two methods (300–350 s). In the case of the April dip ingress data, the template fit to the total light curve is poor, so the estimation from the linear fit to the column density versus time is probably more reliable and therefore the flux change timescale is around 300 s. For the October ingress, the template fit is acceptable, and the light curve predicted by the lag method is not an acceptable fit to the data. Thus the flux change timescale is probably most accurately determined from the template fit to the light curve, and is then probably closer to 200 s

than to 300. For the October egress, the lag method gives a smaller estimation for the timescale of flux increase than do the other two methods, and it is significantly smaller than the timescale estimated from fitting the light curves directly. However, the lag method found an unacceptable fit to the empirical model, probably resulting in the underestimation of the timescale for the flux increase. Thus the timescale for the flux increase for the October egress is around 600–700 s, probably significantly longer than the timescale for flux decrease for the October ingress.

5.4.2. *Column Timescale*

The timescale for the column to change τ_F can be determined from the lag fitting and from the light-curve fitting, and ideally the estimations should be the same. This depends on the validity of two key assumptions: the empirical model for the lag fitting and the constant covering fraction hypothesis for the light-curve fitting. Since the column density as a function of time for the ingresses and egresses of the April and October data were all consistent with a straight-line fit, the exponential empirical model is probably justified. The lag fitting method provides the best determination of the timescale for the column to change, since it is not contaminated by the flux change.

For the October ingress, the estimations of τ_F are the same for both methods. Therefore, the data are consistent with a constant covering fraction, the exponential model is justified, and the folding timescale for the change in column is about 100 s. For the egress, however, the estimation of τ_F from the lag fitting method was much smaller than from the light curve fitting method. The straight line fit from the light-curve fitting method is acceptable, but the lag fit is unacceptable. This result may indicate that the assumption of constant covering fraction is not justified. Recall that τ_D values in different energy bands for the egress were not consistent with a constant, another indication that the constant covering fraction hypothesis is not justified. Therefore, for the egress, an accurate estimation of τ_F cannot be made.

For the April ingress and egress, because of the small lags, the lag method could not be used to find τ_F. However, from fitting the light curve, an implied value of τ_F was found to be about 100–150 s, similar to that found from the October ingress observation. If the constant covering hypothesis is justified, lags should have been found in the April data to those in the October data. Although the low flux of the April data makes measuring the lags difficult, examination of Figure 2 shows that the lags in the April ingress and egress data are smaller than those in the October ingress. Therefore, the constant covering fraction hypothesis is probably not justified, and τ_F cannot be accurately measured from these data. However, the small lags seem to show that it is smaller than for the October ingress.

5.5. *Spectra Predicted by the Model*

The variable-absorption model is designed to explain the lags found in the ingress and egress data sections from the October observation. The hardening of spectra and the larger equivalent widths at low flux can also be qualitatively explained by this model.

To illustrate this, spectra were simulated using the column densities implied by the linear fit of the column density versus time listed in Table 5. The most striking spectral variability occurred between the SOFT and HARD spectra, so these were simulated. A partial-covering spectral model was assumed,

with the intrinsic Galactic column density. A narrow iron line at 6.4 keV with intrinsic equivalent width of 300 eV was added. The covering fraction used was the same as in the previous section. The index was chosen to be 1.54, assumed to approximate the intrinsic photon index, because of an interpretation of the SOFT spectrum. Extrapolating the linear fit to the time at which this spectrum occurs, the variable column becomes large enough to be effectively optically thick. The only effect of the variable column at this time is to attenuate the flux, and only the intrinsic spectrum is seen. Spectra were simulated using XSPEC, so that the energy resolution would be appropriate for the LAC, at 32 s intervals. Since the LAC background is a substantial fraction of the raw data, the uncertainties in the spectra were increased to simulate the Poisson statistics of the background plus the source flux. Finally, these spectra were added together to form simulations of the HARD and SOFT spectra, and examples of these are shown in the upper panel of Figure 10, with the upper spectrum corresponding to the HARD spectrum and the lower corresponding to the SOFT spectrum. For comparison, the same model spectra were integrated over the appropriate range in column density. These are shown in the lower panel of Figure 10. These spectra are essentially the same as those simulated, except that the energy resolution and the effective area of the LAC have not been folded in.

The simulated spectra were fitted with a power law plus absorption and narrow line model. The best-fit photon index and line equivalent width for the SOFT example spectrum were 1.53 and 315 eV, respectively, nearly the input values. In contrast, the best-fit index and line equivalent width for the HARD example spectrum were 1.1 and 410 eV, respectively, and the absorption was measured to be smaller than the intrinsic Galactic column. Therefore, the index was found to be smaller,

the absorption lower, and the equivalent width larger for the spectrum simulated, while the variable absorption was not completely thick. The reasons for this result are seen in Figure 10. In both the upper and lower panels, the upper curve illustrating the simulated HARD spectrum appears slightly flatter due to the superposition of variable column, resulting in the lower index. There is a slight upturn toward low energies, resulting in the smaller absorption measured. This moderation in slope at low energies can also explain the lower column densities found from the low-flux spectra, in both the April and October data. In addition, integration over varying N_H has been shown to produce spectra that turn up at low energies (Parmar et al. 1986). Finally, the lower panel shows a substantial iron edge in the simulated HARD spectrum, which does not appear in the data. Because of the moderate energy resolution of the LAC and the short accumulation time for these spectra, the iron line and iron edge are coupled in spectral fitting. If the iron edge is not explicitly included in the fitting, the iron-line flux measured is augmented. This effect would apply especially to this spectrum, because the variable absorption causes an upturn in the spectrum from about 5 keV toward higher energies, as well as the edge. If such a spectrum is fitted with an iron line and continuum, the iron line will be apparently augmented because of the deficits in flux around it. Thus the large equivalent widths found in the low-flux spectra from the ingress and egress are not physical but only apparent.

Since the flux and accumulation time are small, errors cannot be derived from the example spectra, but require multiple simulations to compute. These computations are beyond the scope of this paper. However, these example spectra illustrate the point that the variable absorption causes the spectral index to flatten and the measured equivalent width to rise when the spectrum is accumulated during the time when the column density is not completely thick but changing.

6. DISCUSSION

6.1. *Summary of Results*

Analysis of the regions of most rapid variability from two *Ginga* observations of NGC 6814 have yielded results which have helped us gain insight into the cause of the most rapid variability in this source. The analysis results are summarized as follows.

Cross-correlations and template fitting analysis discovered significant flux lags from tens of seconds, in the case of the April dip data, to hundreds of seconds, in the case of the October ingress and egress data. The sense of the flux lags was that the hard flux lagged the soft flux during flux decreases and the soft flux lagged the hard flux during flux increases.

The results from the spectral analysis are consistent with the results from the time series analysis. Significant (90%–99% confidence) spectral hardening occurred during the dips of the April observation. Hardening was also discovered during the October ingress as the flux decreased, and softening during the October egress as the flux increased. Rapid marginally significant spectral softening occurred at lowest flux levels of the ingress. The rapid changes in index were generally not accompanied by significant changes in absorption column, although in some cases fits of hard spectra found the Galactic N_H value as the upper limit.

Spectral fitting of the data during the dips of flux from the April observation found that the iron-line flux decreased significantly. The upper limit of the iron-line flux during the dips
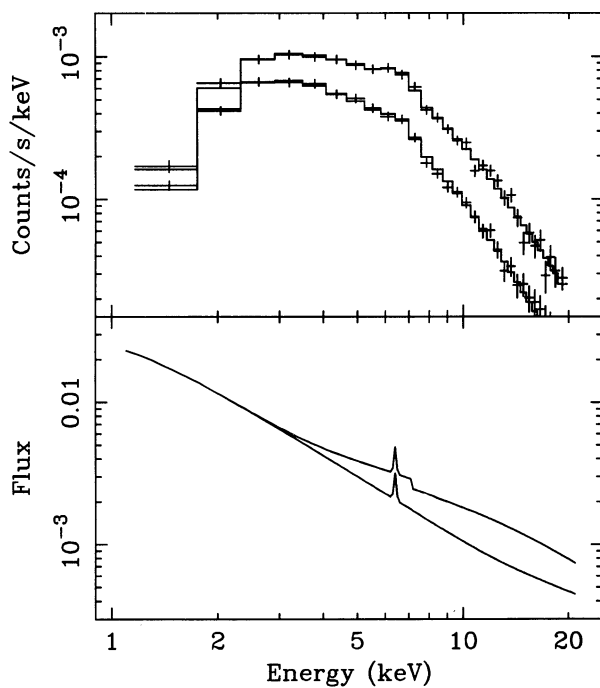

FIG. 10.—Simulated spectra for the ingress and the egress, found using the results of the linear fit to the column density vs. time for the October data. The upper panel shows simulated HARD (*upper*) and SOFT (*lower*) spectra which have had the response and background statistics of the LAC folded in. The best-fit power law plus line and absorption are shown. The lower panel shows the simulated spectra without the response and statistics folded in.

was 0.26 counts s^{-1}. If the total iron-line flux during nondip regions is taken to be 1.5 counts s^{-1} (found in fitting the A1B1, A1B2, and A2B spectra), it is implied that at least five-sixths of the iron emitting region is covered. In contrast, although the iron-line flux decreased in the October data, the equivalent width was found to apparently increase, because of coupling in spectral fitting between the iron line and edge.

6.2. Consistency of the Variable-Absorption Model

Bearing these results in mind, we showed that an empirical functional form of a variable-absorption model could be fitted explicitly to the template fitting data from the October ingress and egress. This model hypothesized the column density to be a two-parameter exponential function of time. Further, the column density as a function of time was derived from the light curves directly, for the average April dip data as well as for the ingress and egress data. It was shown that this model could qualitatively explain the spectral variability of the October data. This model can be used to explain the results from both observations by adjusting two basic model parameters: the relative fraction of unabsorbed flux and the gradient with respect to time of the column.

The flux decreases and subsequent increases in both observations can be explained by the occultation of the source by optically thick material. In the case of the April dips, as the flux decreases to zero, the covering of the source is complete, while in the case of the October ingress and egress, only a fraction of the source is completely occulted, resulting in residual flux at the lowest flux levels.

Further, not only optically thick material is inferred to be present. The lags in flux found can be attributed to surrounding material in which the column density varies continuously from optically thick to effectively zero, excluding the column of the host galaxy. The lags result from the energy dependence of the absorption cross section and the variation of column density. When the variable column changes with a larger gradient with respect to time, the lags are small, as found in the April dip data. This result predicts that the order-of-magnitude folding timescale τ_F of equation (8) would be smaller. When the column varies with smaller gradient, the lags are larger, as found in the October ingress and egress data. The fact that the hard flux falls and recovers so quickly in the dips of the April observation, as shown in Figure 2, illustrates that the time-variable absorbing material implied by the variable-absorption model must have only a small region which is completely optically thick to X-rays. Indeed, the region occulting the source in hard X-rays must be approximately the size of the source of hard X-rays.

This model can also produce the spectral changes which were found. This is because, when a spectrum is accumulated while the column is changing, an effective integration over a sequence of increasingly absorbed spectra occurs. In contrast to the spectral break which is found in spectra well fitted by a simple partial-covering model, no break is observed in these spectra because of the smooth integration, short accumulation times, and moderate spectral resolution of the LAC. In some cases there can be a low-energy upturn which leads to a measured absorption upper limit consistent with Galactic $N_{\rm H}$. In the April data the hardening of the spectrum during the dips occurs because the integration is performed over a region in which the hard flux is relatively unabsorbed, except at the cusp of the dip, while the low and median fluxes are more absorbed to varying degrees. The spectral change is found to be signifi-

cant with high confidence, since the variation was so fast and since only absorbed spectra are seen. But because the column changes with a shorter timescale compared with the spectral binning, only flattening is observed, with no significant increase in column density. In the October data, where the gradient of the column is smaller and where there is an added fraction of unabsorbed flux, the gradual hardening of the spectrum which would be expected is found explicitly in the spectral fitting results. The spectral hardening is not found to be significant with high confidence, both because, since the source is only partially occulted, a fraction of unabsorbed flux contributes to the absorbed flux, and because the hardening is more gradual. The fast, moderately significant spectral softening found at the lowest flux level can be attributed to the partial occultation by the source only by material which is optically thick.

The changes in the iron-line emission can also be explained by this model. Partial occultation of the line emission region can explain the significant decrease in the line flux found in the April data. That such a significant decrease is not found in the October data may be due to the fact that in the October data the source is inferred to be only partially covered and therefore the line emission region may be correspondingly less covered. The large equivalent widths found at low fluxes in the October data can be attributed to a coupling in the spectral fitting of the iron line with the iron absorption edge and low-energy upturn predicted in the absorbed spectra, and thus are only apparent. Therefore, excepting the region of the dip where the line was not required in the fitting, and covering of the line emission region is inferred, the equivalent width is constant.

6.3. Competing Physical Processes

Since the question of the nature of the most rapid variability in NGC 6814 as been of interest ever since it was discovered, it is necessary to examine the possible competing physical models in order to demonstrate why they could not adequately explain the observations. This is especially true, since several models can predict flux-correlated spectral variability, and usually these models cannot be differentiated by the spectra from present detectors with moderate energy resolution.

The types of models competing with the variable-absorption model presented in this paper fall naturally into two types: those in which the variability is due to intrinsically variable flux and those in which the variability is due to ionization of the absorption column (warm absorber).

6.3.1. Intrinsic Variability

The X-ray power law is believed possibly to be produced by the upscattering of soft photons by energetic electrons. Adjusting the model parameters changes both the spectrum and the flux. However, the major objection to such a model as the source of the rapid variability of NGC 6814 is provided by the evidence of the April dips. The fact that the flux drops to zero would be difficult to explain by an intrinsic process, since it would be equivalent to turning off the source of X-rays.

A natural model which can produce spectral variability during flux changes is a thermal Compton model, in which the X-ray power law is produced by upscattering of soft photons by energetic thermal electrons (e.g., Shapiro et al. 1976). This model is easily ruled out by the results of the data analysis. Thermal Compton models predict lags (Lightman, Giacconi, & Tananbaum 1978); however, the sense of the lag must be such that the hard flux always lags the soft flux during flux changes,

due to the greater number of collisions necessary to upscatter photons to the highest energies. The sense of the lags in both the April and October egress data is just opposite to this prediction, hence this type of model can be clearly ruled out.

Nonthermal Compton models, in which the X-ray power law is produced by the upscattering of soft photons by a population of nonthermal electrons, can produce spectral variability and lags, in the sense that are observed (Fabian et al. 1986; Done & Fabian 1989). Even the fast spectral softening observed in the October ingress data can be explained. The source has been proposed to be photon-starved by Done et al. (1992), because of the relatively flat spectral index observed. In this case, if there is a sudden burst of soft photons, copious pairs will be produced, and the spectrum can soften rapidly while remaining at approximately the same flux level. However, it would be necessary to provide a soft photon source with rapid variability. If the source of the soft photons is the accretion disk, it is unlikely that the timescale of variability would be so short (C. Done 1991, private communication). An estimation of the minimum timescale for a change in the accretion disk emission would be the dynamical timescale at $\sim 5 r_s$. For a $10^6 M_\odot$ black hole (see § 6.4; Kunieda et al. 1990) this timescale would be ~ 1000 s, an order of magnitude larger than the timescales found here. Also, the temporal behavior predicted by photon-starved models would not be consistent with the lag behavior observed here.

6.3.2. Warm Absorber Models

Spectral variability in some other sources has been explained by a warm absorber model (e.g., Halpern 1984; Yaqoob, Warwick, & Pounds 1989). In such a model, an increase in flux results in the ionization to some degree of the intervening absorbing screen. The moderate ionization reduces the opacity in low energies, and proportionally more soft photons are able to leak through, causing an apparent softening of the spectrum. As a result, the power-law spectral index is found to be correlated with the source flux. In addition, for moderate ionizations warm absorbers can produce quite rapid variability; if the temperature of the gas is less than 10^4 K and the density is 10^{10} cm^{-3}, the timescale for hydrogen recombination would be on the order of hundreds of seconds.

However, this model cannot be applied to the most rapid variability of NGC 6814 for several reasons. First, since the variability is seen in even the highest energy bands, the opacity of the material must change substantially above 7 keV. Iron provides the largest opacity at these energies, but the cross section of the iron edge is similar for all ionization states (George & Fabian 1991). For the change in flux to be produced by a change in ionization, the iron must be very highly ionized, and therefore it will be the only source of opacity. Thus the opacity at high energies is larger than at low energies, and therefore it cannot produce the lags observed. It would also be impossible to explain the sudden softening of the spectrum at lowest flux, since the flux remained approximately constant, and a warm absorber model requires a change in spectrum to be accompanied by a change in flux. Finally, the measured absorption column is not correlated with the flux, as would be expected in the warm absorber model.

6.4. Constraints on General Geometrical Models

It is now well documented that NGC 6814, besides being unique among Seyfert 1 nuclei in its most rapid variability, has also been found to exhibit apparently unique periodic variability (Mittaz & Branduardi-Raymont 1989; Done et al. 1992), with a period of $\sim 12,000$ s. The rapid variability is thus a feature in the periodic component of the light curve. The analysis of the overall variability of both observations will be described in Paper II of this series. Assuming the periodicity of the source, the results presented in this paper are used in the following section to construct a general geometric model. Finally, the implications of these results for existing models is briefly discussed.

6.4.1. Size of the Occulting Material

A first constraint is the size of the covering material, which can be determined independent of the model, by using the shape of the April dip, if relativistic effects are neglected. Since the source is completely occulted, the region of optically thick occulting material must be equal to or larger than the source in projected size. Furthermore, for the hardest flux band, the light curve shown in Figure 2 drops to a cusp, indicating that the source of hard X-rays must be completely covered only for an instant. Thus the source must be the same size as the optically thick part of the cloud. The full width at half-maximum is an estimation of this size, which therefore must be about $300v$, where v is the velocity describing the occultation. The flat bottom of the low-energy dip light curve indicates that the soft source of photons is covered for about 100 s longer than the hard source, indicating a region of optically thin ($\sim 10^{23}$ cm^{-2}) absorbing material about $100v$ larger than the soft photon source. This size is consistent with the lags being on the order of ~ 50 s. For the October data, the extended region must be at least an additional $200v$ larger to account for the larger lags. This estimation is consistent with the timescale of column change for the October ingress being about 100 s.

6.4.2. Size of the Iron-Line Emitting Region

All occultation models require the bulk of the iron-line emission to come from a region very close to the central source, since spectral fitting of the April dip data found the line flux decreased significantly. Therefore, the iron-line producing region is assumed to be mostly occulted also. In order to explain the large equivalent width and rapidly varying iron line, as well as the apparent lack of a hard reflection component, it has been suggested that the line comes from ionized gas within the X-ray source region. Since the gas is ionized, the fluorescence yield is enhanced, but the emission energy is also ~ 6.7 keV and therefore must be redshifted to an energy approximately that of neutral iron (Turner et al. 1992; Hayakawa 1991).

6.4.3. Position of the Occulting Material

The simplest periodic occultation model is that in which the source is occulted by an orbiting cloud. The results of the analysis allow us to place severe constraints on the cloud material, as follows.

First, the black hole mass must be determined. The source size is approximately $300v$. The bulk of the primary radiation should be produced within $10 r_s$ (e.g., Shapiro et al. 1976). Therefore, an upper limit on the black hole mass of 3×10^6 $M_\odot$ is obtained by replacing v by the speed of light. However, note that if the geometry is highly inclined, and if the source of X-rays is just the inner edge of the accretion disk, the radiation must be beamed toward us and the source can appear much smaller (Cunningham & Bardeen 1972). In that case, the black hole mass would be allowed to be larger, although the physical constraints on the absorbing material would be even more

restrictive (S. Chakrabarti 1993, private communication). It is also possible that the source is substantially smaller than $10r_S$, reducing the implied upper limit. The lower limit comes from requiring the luminosity to be less than the Eddington luminosity. The 2–20 keV luminosity of NGC 6814 is about 7×10^{42} ergs s^{-1} (Kunieda et al. 1990). However, the bolometric luminosity may be 10 times larger than that (Padovani & Rafanelli 1988). Requiring that the luminosity not exceed the Eddington luminosity results in $M_{bh} > 5.6 \times 10^5 M_\odot$.

A reasonable median value is $10^6 M_\odot$. This size has been found by other authors using different methods (Tennant et al. 1983; Mittaz & Branduardi-Raymont 1989; Kunieda et al. 1990). If the velocity is Keplerian, the distance to the occulting material is $R = 27r_S = 8 \times 10^{12}$ cm. The velocity of the orbiting material is $0.14c$, and the extent of the optically thick portion of the cloud is about 1.25×10^{12} cm.

6.4.4. Ionization of the Occulting Material

The orbiting and occulting material is subject to a strong radiation field. However, the results of the data analysis require that the material be not substantially ionized, in order to produce the lags observed. Thus the ionization parameter

$$\xi = \frac{L}{nR^2}, \qquad (10)$$

where n is the number density of the material, should not be larger than about 100 (Kallman & McCray 1982), so that oxygen, which provides the bulk of photoelectric absorption at low energies above 0.53 keV, should not be largely ionized.

An orbiting spherical cloud could possibly approximate an exponential change in column density if the radial number density were an appropriate function. The thickness of the cloud would be about the same as the extent, approximately 1.25×10^{12} cm. If the extended region, which absorbs soft photons, is assumed to be on the projected edge of the cloud, a moderate column of 10^{23} cm^{-2} would be attained with a geometrical thickness of 10^{12} cm. The number density in the cloud would be required to be $\sim 10^{11}$ cm^{-3}, but the ionization parameter would be $\xi \approx 10^7$, and the material would be ionized. Using the bolometric luminosity rather than the ionizing luminosity only overestimates by a factor of 10. Thus this simplest model cannot be consistent with the observations.

Alternatively, if the ionization parameter is required to be less than 100, then the density of the material must be $\geq 10^{16}$ cm^{-3}. Note, however, that at these large densities, the ionization parameter cannot be applied completely reliably (Ferland & Rees 1988), because of additional microphysical processes which have the effect of pushing the material into a more nearly neutral state. The effect of this result is that high-density material becomes a more efficient photoelectric absorber (Ferland & Rees 1988). Thus it may be true that the density of the material need not be quite so high. Note also that it can be shown that clouds with such properties obey the Guilbert & Rees (1988) criterion given in equation (6) of that publication, implying that the clouds are able to cool adequately by bremsstrahlung.

If the number density is 10^{16} cm^{-3}, then for a column density of 10^{23} cm^{-2} at about the middle of the variably absorbing region, the physical thickness would be only 10^7 cm. Thus, with the extent of the variably absorbing region being about $100v = 4 \times 10^{11}$ cm, the geometrical thickness of the region would be less than 1/10,000 of the extent. Thus the

shape of the occulting material would be very sheetlike, lying roughly perpendicular to the radial direction.

Such material has been hypothesized to exist near the central engine (Rees 1987; Guilbert & Rees 1988; Celloti, Fabian, & Rees 1992). In fact, the geometry of the material has been predicted to be filamentary or sheetlike. This is because a tangled magnetic field is supposed to provide the confining pressure to support such densities, and the clouds are highly compressed in one direction. If the magnetic field is assumed to be in equipartition with the accretion energy, and assuming a conversion of gravitational energy to accretion energy of $\eta \approx 0.1$, the magnetic pressure available at this radius would be as large as $P_B = 1.7 \times 10^6$ ergs cm^{-3}. This would be more than 10 times the pressure required to confine material with density $n \approx 10^{16}$ cm^{-3}, even if the temperature were as high as 1 rydberg.

6.5. Current Physical Models

The periodicity observed in the X-ray light curve of this source has stimulated the production of several models to explain this effect. These models include an orbiting screen model (Done et al. 1992), a rotating hot spot model (Abramowicz 1992), and occultation by nondisk structures caused by interaction of orbiting objects in the plane of the accretion disk (Syer, Clarke, & Rees 1991; Sikora & Begelman 1992; King & Done 1993). Here the implications of the results presented in this paper on these models is briefly discussed.

6.5.1. Constraints on Screen Models

A type of orbiting model which has been proposed is an orbiting screen model (Done et al. 1992). This screen is assumed to be in the form of a geometrically thick disk with a funnel-shaped interior. It is then the edge of the funnel which is able to occult the source.

If this thick disk is a radiation-supported torus (Madau 1988), then this type of model is severely constrained by our data. The radiation torus is generally supported by radiation pressure and is assumed to be highly ionized. The characteristic temperatures and densities show that the electron scattering opacity must dominate, and, since the material is ionized, bound-free opacity will not be important. Since electron scattering opacity is energy-independent at the energies that we examine, such models which have occultation due to material dominated by electron scattering cannot produce the lags observed.

6.5.2. Constraints on Hot Spot Models

The orbiting hot spot model (Abramowicz 1992) has been successfully used to explain the periodic flaring found in the long EXOSAT observation of this source. In this case, an orbiting emitter was proposed to be modified and enhanced by Doppler effects and gravitational lensing.

Such a model can also admit absorption, if the absorbing screen is relatively stationary and the hot spot is rotating behind it. However, there may be an inconsistency. First, although there are flaring and dips observed in the October observation, there are no extremely large flares that would point to the existence of only one spot. On the other hand, if there were several spots, they must be orbiting with nearly the same period, because the primary component to the variability power is the periodic component (Done et al. 1992). In that case, each would be occulted behind the same variable-absorption screen; then they would all necessarily exhibit

similar spectral variability as they were occulted. However, when the hardness ratio is examined, it can be shown that although there are other flux increases and decreases in the light curve, as shown in Figure 1, only the ingress and egress exhibit such large and fast changes in hardness ratio.

6.5.3. *Constraints on Orbiting Star Models*

A final model is that of an orbiting star or compact object (Syer et al. 1991; Sikora & Begelman 1992; King & Done 1993). According to Sikora & Begelman (1992), a star would be orbiting the black hole at an angle to the accretion disk. As the star crosses the disk plane, material will be shocked out of the plane of the disk. The variability could be provided by the occultation by the ejected material, formed at impact and orbited into view. The lags observed could be provided by the material with smaller projected column density surrounding the plug. The constraint would be the relatively low degree of ionization required. It is difficult to determine the properties of this material, as it would be far from equilibrium. Since the plug is re-formed at every orbit, the structure need not be particularly stable. As the orbit of the star can be expected to precess, the differing shape of the light curves can be expected at timescales of 6 months to a year (Sikora & Begelman 1992).

7. SUMMARY

We have examined in detail the spectral and temporal behavior of NGC 6814 around the regions of most rapid variability through analysis of two *Ginga* observations. A detailed analysis around the most rapidly variable parts of the light curve found spectral variability and lags in flux between different energy bands. Lags were on the order of a few to tens of seconds for the April data, and on the order of tens to a couple of hundred seconds for the October data. During flux decreases the hard flux lagged, while during flux increases the soft flux lagged. Apparent hardening of the spectrum at low flux was observed in the April data. Apparent hardening of the spectrum also occurred in the October flux decrease, to a photon index of $\Gamma = 0.85$; however, the spectrum softened at lowest flux to the index of the predecrease level, $\Gamma = 1.54$. In the April dips the line flux was found to decrease significantly. A marginal decrease in line flux was also observed in the October data.

We hypothesized that the lags could be explained if the column covering the source was changing with time. To test this hypothesis, the implied time dependence of the column was determined in two ways. First, the time dependence of the column density was assumed to be exponential, and the times at which the flux falls halfway between the initial and final value obtained from template fitting to light curves in different energy bands were compared with those expected from a two-parameter exponential model. This method uses only the information of the lag data to compute the time dependence of the column density. The second method used the information pro-

vided by the change in flux also. A partial-covering spectral model with constant covering fraction was assumed, and simulated light curves were generated. These were compared with the data, and column densities as a function of time were generated for several energy bands. For a variable column to be the cause of the flux change, the column densities obtained at different energies must be consistent with one another. Thus, at each time, a constant column was fitted. These plots of the log of the column versus time were then fitted with analytical models. Straight lines provided a good fit in most cases, indicating that the assumption of an exponential model was justified. The flux change timescales could be estimated from the lag fitting, the light-curve fitting, and the template fitting of the total light curve. The flux change timescales for the April dip ingress and egress were found to be about 300–350 s in both cases. For the October ingress, the template fitting offered the most reliable estimate of the flux change timescale of ~ 200 s. For the October egress, the flux change timescale was larger, around 600–700 s. The column change folding timescale of 100 s was estimated for the October ingress data, while for the April dip and October egress data, the column change timescale could not be estimated reliably.

The spectral variability could be qualitatively explained by the variable-absorption model. Simulations demonstrated that when the source was covered by the variable column that was not completely optically thick, the spectrum flattened, the apparent intrinsic column decreased, and the line equivalent width increased as observed because of the coupling of the iron edge with the iron line in the low-resolution data.

If the absorber is material orbiting a black hole, restrictive physical conditions are required. This is mostly due to the fact that the lags require the absorption to be photoelectric, and so the ionization state must be relatively low ($\xi < 100$) for oxygen to not be ionized. At $\sim 30 r_s$, because of the large X-ray flux, the material must be therefore very dense ($n > 10^{16}$ cm^{-3}). Consideration of the extent of the variable column as implied by the lags forces the conclusion that the material must have a sheetlike geometry, extending much farther azimuthally than radially.

APPENDIX

The *Ginga* mission and the large-area counter (LAC) are described in Turner et al. (1989). During these observations, the LAC was operated in the MPC-1 mode in order to obtain good spectral information and moderate time resolution of 16 s.

Careful and conservative data selection was employed, in order to minimize possible systematic background subtraction error. Only data from low-background orbits were used, chosen during times when the satellite would not pass through the high-background region of the South Atlantic Anomaly (SAA). Data were chosen only from regions where the Earth elevation angle was greater than 6°, avoiding possible solar X-ray reflection off the Earth's atmosphere. Only data having a large geomagnetic cutoff

LEIGHLY ET AL.

rigidity greater than 9 GeV/c were chosen, avoiding contamination by particle background. Finally, since it has been shown that the SSUD count rate (surplus count rate over upper discriminator greater than 37 keV) scales with the background count rate (Hayashida et al. 1989), only data with low SSUD were used.

The usual observational procedure includes a background observation from an adjacent area of sky with no X-ray point sources, accumulated for one day before and/or after the source observation. The background spectrum has variable shape and amplitude depending on the amount of time elapsed after the satellite emerges from the high-background region of the SAA (Hayashida et al. 1989). Since the SSUD count rate scales with the background, the usual method of background subtraction proceeds by accumulating several background spectra at different SSUD rate levels, and then subtracting these from source spectra collected with the same SSUD rate. To produce time series, this process proceeds one step further: a quadratic function of the background spectra is used to determine the appropriate count rate at each energy and for each 16 s time bin. This background subtraction method was used for the October observation.

For the April observation, no adjacent background observation was performed. Therefore two methods of background subtraction were used. To produce spectra, characteristic diffuse and internal background spectra were used, accumulated over large amounts of time. The internal background spectra were scaled to the source spectra amplitude using the SSUD count rate and the count rate of the midlayer detector at energies less than 5 keV, where the effective area is negligible. The scaled internal background and the average diffuse background spectra were then subtracted from the source spectra. This method is explained in detail in Awaki et al. (1991). For the production of the time series, this method was not available. Therefore, a background observation performed on 1990 March 9, 37 days previous to the observation, was found, and the SSUD scaled background subtraction method explained above was used. A background observation at that time is appropriate because the small eccentricity of the satellite causes the elevation of the satellite as it passes through the South Atlantic Anomaly to vary with 37 day periodicity.

Finally, the energy calibration of each detector was checked by fitting the position of the 22.1 keV silver line. Also, the aspect was accounted for in both the time series and spectral data, including correction for low-energy collimator-reflected X-rays. Only data with transmission coefficient $T > 0.5$ were used for spectral fitting. In this paper, spectral fitting was performed from 2.8 to 20.9 keV, in order to avoid an apparent soft excess component. Only the top-layer data were used for spectral fitting. For time series analysis, data were accumulated from both the top layers and the midlayers together, from 1.11 to 20.9 keV.

REFERENCES

Abramowicz, M. A. 1992, in Testing the AGN Paradigm, ed. S. S. Holt, S. G. Neff, & C. M. Urry (New York: AIP), 69
Awaki, H., Koyama, K., Inoue, H., & Halpern, J. P. 1991, PASJ, 43, 195
Celloti, A., Fabian, A. C., & Rees, M. J. 1992, MNRAS, 255, 41
Clavel, J., et al. 1991, ApJ, 366, 64
Cunningham, C. T., & Bardeen, J. M. 1972, ApJ, 173, L137
Done, C., & Fabian, A. C. 1989, MNRAS, 240, 81
Done, C., Madejski, G. M., Mushotzky, R. F., Turner, T. J., Koyama, K., & Kunieda, H. 1992, ApJ, 400, 138
Edelson, R. A., & Krolik, J. H. 1988, ApJ, 333, 646
Fabian, A. C., Blandford, R. D., Guilbert, P. W., Phinney, E. S., & Cueller, L. 1986, MNRAS, 221, 931
Ferland, G. J., & Rees, M. J. 1988, ApJ, 332, 141
George, I. M., & Fabian, A. C. 1991, MNRAS, 249, 352
Guilbert, P. W., & Rees, M. J. 1988, MNRAS, 233, 475
Halpern, J. P. 1984, ApJ, 281, 90
Hayakawa, S. 1991, Nature, 351, 214
Hayashida, K., et al. 1989, PASJ, 41, 373
Kaastra, J. S., & Barr, P. 1989, A&A, 226, 59
Kallman, T. R., & McCray, R. 1982, ApJS, 50, 263
King, A., & Done, C. 1993, MNRAS, in press
Kunieda, H., Hayakawa, S., Koyama, K., Tawara, Y., Tsuruta, S., & Leighly, K. 1992, ApJ, 384, 482
Kunieda, H., et al. 1991, in Iron Line Diagnostics in X-ray Sources, ed. A. Treves, G. C. Perola, & L. Stella (Berlin: Springer-Verlag), 241
Kunieda, H., Turner, T. J., Awaki, H., Koyama, K., Mushotzky, R. F., & Tsusaka, Y. 1990, Nature, 345, 786

Lampton, M., Margon, B., & Bowyer, S. 1976, ApJ, 208, 177
Leighly, K. 1991, Ph.D. thesis, Montana State Univ.
Leighly, K., Kunieda, H., & Tsuruta, 1992, in Testing the AGN Paradigm, ed. S. S. Holt, S. G. Neff, & C. M. Urry (New York: AIP), 93
Lightman, A. P., Giacconi, R., & Tananbaum, H. 1978, ApJ, 224, 375
Madau, P. 1988, ApJ, 327, 116
Makino, R., & the ASTRO-C Team. 1987, Astrophys. Lett. Comm., 25, 223
Matsuoka, M., Yamauchi, M., Piro, L., & Murakami, T. 1990, ApJ, 361, 440
McHardy, I., & Czerny, B. 1987, Nature, 325, 696
Mittaz, J. P. D., & Branduardi-Raymont, G. 1989, MNRAS, 238, 1029
Morrison, R., & McCammon, D. 1983, ApJ, 270, 119
Nandra, K., Pounds, K. A., & Stewart, G. C. 1990, MNRAS, 242, 660
Padovani, P., & Rafenelli, P. 1988, A&A, 205, 53
Parmar, A. N. White, N. E., Giommi, P., & Gottwald, M. 1986, ApJ, 308, 119
Pounds, K. A., Turner, T. J., & Warwick, R. S. 1986, MNRAS, 211, 7P
Rees, M. J. 1987, MNRAS, 228, 47P
Shapiro, S. L., Lightman, A. P., & Eardley, D M. 1976, ApJ, 204, 187
Sikora, M., & Begelman, M. C. 1992, Nature, 356, 224
Syer, D., Clarke, C. J., & Rees, M. J. 1991, MNRAS, 250, 505
Tennant, A. F., & Mushotzky, R. F. 1983, ApJ, 264, 92
Tennant, A. F., Mushotzky, R. F., Boldt, E. A., & Swank, J. H. 1981, ApJ, 251, 15
Turner, M. I. L., et al. 1989, PASJ, 41, 345
Turner, T. J., Done, C., Mushotzky, R. F., Madejski, G. M., & Kunieda, H. 1992, ApJ, 391, 102
Turner, T. J., & Pounds, K. A. 1988, MNRAS, 232, 463
Yaqoob, T., Warwick, R. S., & Pounds, K. A. 1989, MNRAS, 236, 153

Note added in proof.—A recent *ROSAT* observation of the NGC 6814 field has revealed that much of the variable X-ray emission previously attributed to the Seyfert galaxy actually originates from a Galactic accreting binary object offset by 0″.37 (G. M. Madejski et al., Nature, in press [1993]).